Jinst

Published by IOP Publishing for Sissa Medialab

Received: *September 9, 2022*
Revised: *July 10, 2023*
Accepted: *September 10, 2023*
Published: *September 28, 2023*

List-mode quantitative joint reconstruction of activity and attenuation maps in Time-of-Flight PET

Hamidreza Hemmati,[a,b] **Alireza Kamali-Asl,**[c] **Pardis Ghafarian,**[d,e] **Arman Rahmim,**[f,g] **Habib Zaidi**[h,i,j,k,*] **and Mohammad Reza Ay**[a,l,*]

[a] *Research Center for Molecular and Cellular Imaging, Tehran University of Medical Sciences, Tehran, Iran*
[b] *Department of Biomedical Engineering, University of California, Davis, Davis, CA, U.S.A.*
[c] *Department of Medical Radiation Engineering, Shahid Beheshti University, Tehran, Iran*
[d] *Chronic Respiratory Disease Research Center, NRITLD, Masih Daneshvari Hospital, Shahid Beheshti University of Medical Sciences, Tehran, Iran*
[e] *PET/CT and Cyclotron Center, Masih Daneshvari Hospital, Shahid Beheshti University of Medical Sciences, Tehran, Iran*
[f] *Departments of Radiology and Physics, University of British Columbia, Vancouver, BC, Canada*
[g] *Department of Integrative Oncology, BC Cancer Research Centre, Vancouver, BC, Canada*
[h] *Division of Nuclear Medicine and Molecular Imaging, Geneva University Hospital, Geneva, Switzerland*
[i] *Geneva University Neurocenter, Geneva University, Geneva, Switzerland*
[j] *Department of Nuclear Medicine and Molecular Imaging, University of Groningen, University Medical Center Groningen, Groningen, Netherlands*
[k] *Department of Nuclear Medicine, University of Southern Denmark, Odense, Denmark*
[l] *Department of Medical Physics and Biomedical Engineering, Tehran University of Medical Sciences, Tehran, Iran*

E-mail: habib.zaidi@hcuge.ch, mohammadreza_ay@tums.ac.ir

Abstract: Quantitative PET imaging requires accurate determination of patient-specific attenuation maps, which remains challenging on hybrid PET/MRI systems owing to the lack of a direct

*Corresponding author.

https://doi.org/10.1088/1748-0221/18/09/P09041

2023 JINST 18 P09041

relationship between MR image intensity and attenuation coefficients. The aim of the present study is to develop a list-mode based algorithm for accurate and robust attenuation correction of PET data using time-of-flight (TOF) emission information. We analyze and address the challenges of list-mode emission-based maximum-likelihood joint estimation of activity and attenuation (LM-MLAA) in state-of-the-art PET imaging. The proposed method exploits a rapid on-the-fly system matrix calculation algorithm based on elliptic integrals while updating the attenuation map from accumulating list-mode coincidences to achieve accelerated image reconstruction. The scattering compensation is incorporated inside it using an iterative approach in such that the current estimation of attenuation map used on a course grid sampling scattering points to make an estimate of scattering. The performance of the proposed LM-MLAA approach was evaluated on Monte Carlo simulations of a phantom at different time resolutions. The contrast and noise for hot and cold regions on reconstructed images at different time resolutions were analysed. The estimated attenuation map exhibits resilience against noise, effectively eliminates high-frequency cross-talk even in the absence of prior information on attenuation coefficients, and enables discrimination among different anatomical regions in the reconstructed image. The error in the mean estimated attenuation coefficients after 50 iterations was $\sim 2\%$ in water and $\sim -14\%$ in Teflon regions for TOF resolutions corresponding to those of most current commercial PET systems (~ 500 ps). The proposed LM-MLAA framework can be used for joint reconstruction of activity and attenuation maps from list-mode emission data as standalone or a complementary approach to existing in multimodality imaging such as PET/MRI, where direct measurement attenuation maps is not possible.

Keywords: Gamma camera, SPECT, PET PET/CT, coronary CT angiography (CTA); Medical-image reconstruction methods and algorithms, computer-aided diagnosis; Multi-modality systems

2023 JINST 18 P09041

Contents

2023 JINST 18 P09041

1 Introduction

Correction for photon attenuation within the patient's body is an essential step in the reconstruction of quantitative PET images [1]. Accurate attenuation correction in PET requires the utilization of a patient-specific attenuation map. In the context of hybrid PET/CT systems, CT images have become the standard for deriving attenuation maps due to the strong correlation between electron density and attenuation coefficients. However, the situation differs in PET/MR imaging systems [2]. Unlike CT, there is no direct relationship between the MRI signal and attenuation coefficients since MRI signals are primarily influenced by proton density and tissue relaxation times. Consequently, addressing this challenge necessitates the exploration of various approaches. To tackle this challenge, several approaches have been proposed, including MR image segmentation-based techniques that partition the body into tissue classes with different attenuation characteristics, atlas-based and machine learning techniques where co-registered CT-MR image pairs combined with a mapping/learning technique to derive pseudo-CT images and emission- and transmission-based techniques that exploit TOF emission or transmission data [2, 3]. The conceptual basis of the emission-based approach lies in the fact that emission PET data contains important information about the attenuation map. Unlike CT-based attenuation map estimation, emission-based approaches for attenuation map generation do not require energy mapping [5]. Instead of relying on CT images, the co-registration

of attenuation and emission images can be employed on emission based methods when CT data is not available. This allows for accurate attenuation map estimation even in scenarios where a dedicated CT scan is not feasible or practical. The attenuation information can be extracted based on consistency conditions or simultaneous estimation of activity and attenuation maps in a Maximum Likelihood (ML) framework [2, 4]. The Maximum Likelihood reconstruction of Activity and Attenuation (MLAA) proposed by Nuyts et al. uses a constrained ML approach for simultaneous reconstruction of activity and attenuation maps from emission data [5]. The cross-talk (where some features of the activity map propagate into the attenuation map and vice versa) confines the use and application of the MLAA framework in PET. It has been shown that TOF PET reconstruction is less sensitive than non-TOF reconstruction to inconsistent normalization and inaccurate data correction, and hence is capable of suppressing or at least reducing cross-talk in MLAA [6, 7]. The elegant mathematical analysis revealed that the attenuation coefficients in support of the emission sinogram can be determined from emission data up to a constant scaling factor in TOF PET [8]. Incorporation of prior knowledge on the attenuation map can confine the local convergence of the likelihood function and also reduce the cross-talk error and noise in the resulting images. The prior information can be determined in the form of connected regions from MR images [9], local smoothness of the attenuation map [5], histogram-based priors [4, 10] and scatter coincidences based information [11, 12].

Conventional PET reconstruction approaches bin the acquired data into sinogram bins. In this scenario, each detected coincidence is stored at one of predetermined detector locations (or bins), and each bin only represents the total number of counts for the LORs that have been grouped together based upon common characteristics. Also, rebinning methods can be used for further reduction of the dimensionality of the data and speed-up 3D reconstruction. The incorporation of TOF information in 3D PET adds an additional dimension to the acquired dataset. Application of data mashing may degrade image quality (spatial resolution), especially away from the center of the FOV [13] due to the integration of nearby LORs into the same sinogram bin. Moreover, random and scattered coincidences need to be critically considered and integrated into the forward projection operator of iterative reconstruction because they may yield negative sinogram bins when subtracted from the measured data. List-mode reconstruction is valuable in PET applications where there is a need for high spatial and/or temporal resolution, such as high-resolution small-animal or organ-specific imaging, as well as for dynamic studies. In addition, list-mode reconstruction is more useful than the histogramming mode in terms of storage requirements, especially for high-resolution PET [13]. Furthermore, list-mode reconstructions can naturally incorporate motion correction of the individual events during the reconstruction process [14]. To the best of our knowledge, no practical list mode based MLAA was implemented so far. Yet, Rezaei et al. extended the sinogram implementation of the MLAA algorithm to handle list mode data [15]. In the work of Rezaei et al., the authors compared visually list mode and sinogram reconstructions of a NEMA phantom, though no quantitative analysis was performed. In addition, corrections for scatter or random coincidences were not considered. Moreover, user interaction was suggested to constrain the attenuation map estimation in regions with no tracer uptake. In the present work, we propose a list-mode TOF MLAA algorithm (LM-MLAA) with internally scatter compensation on an iterative approach for simultaneous reconstruction of activity and attenuation maps from emission data. This method is able to cope with the considerable size of list mode data generated from fully 3D TOF PET acquisitions.

2023 JINST 18 P09041

2 Materials and methods

2.1 Principle of MLAA

In TOF PET, the mean number of detected coincidences for LOR i with associated detection photon time difference t, $\overline{g}_{it}$, is expressed as:

$$\overline{g}_{it} = n_i e^{-\sum_k l_{ik}\mu_k} \sum_{j=1}^{J} c_{ijt}\lambda_j + n_i \overline{S}_{it} + \overline{r}_{it} \tag{2.1}$$

where λ and μ are the activity and attenuation vectors, respectively, n_i is a normalization factor, the term $e^{-\sum_k l_{ik}\mu_k}$ models photon attenuation, c_{ijt} represent the coefficients of the system matrix (scanner geometry and physical imaging processes) for LOR i, voxel j and TOF bin t, and $\overline{S}_{it}$ and $\overline{r}_{it}$ denote the estimated scattered and random coincidences for the LOR i at TOF bin t. In addition, J represents the number of voxels in the activity map, and l_{ik} denotes the attenuation intersection length for LOR i and voxel k. The activity and attenuation maps can be determined from the measured PET emission data g_{it} using the log-likelihood maximization:

$$\begin{aligned} L(g|(\lambda,\mu)) &= \sum_{it} g_{it} \ln \overline{g}_{it} - \overline{g}_{it} \\ \hat{\lambda}, \hat{\mu} &= \arg\max_{\lambda,\mu} \{L(g|\lambda,\mu) + \alpha P(\mu)\} \end{aligned} \tag{2.2}$$

where L and P denote the objective function corresponding to the logarithm of the likelihood and prior terms for the attenuation map. This prior usually involves knowledge about the attenuation map and can be weighted relative to the original likelihood function using α. The function would not be concave if λ and μ are treated as unknown distributions. For solving this problem, MLAA approach based on the alternate updates of λ and μ was proposed that converges toward a local optimum [5].

2.2 List-mode MLAA

In the list-mode format, the measured data are stored as a list of detector location pairs with additional potential information, such as detected photon energies, TOF, and depth-of-interaction. The attenuation along each LOR i can be described as:

$$a_i^m = \exp\left(-\left(\sum_{b=1}^{J} l_{ib}\mu_b^m\right)\right) \tag{2.3}$$

where m is the iteration number. The list-mode algorithm for activity reconstruction can be formulated as follows [13, 14, 16]:

$$\lambda_j^{m+1} = \frac{\lambda_j^m}{\sum_{i=1}^{I} n_i a_i^m c_{ijt}} \left(\sum_{k=1}^{N} n_{i_k} a_{i_k}^m c_{i_k jt} \frac{1}{(n_{i_k} a_{i_k}^m \sum_{b=1}^{J} c_{i_k bt}\lambda_b^m) + \overline{s}_{i_k t} + \overline{r}_{i_k}}\right) \tag{2.4}$$

where i_k is the corresponding LOR of the k^{th} list-mode event, N is the total number of measured events, I denotes the total number of possible LORs. The log-likelihood for transmission tomography

2023 JINST 18 P09041

keeping λ constant can be calculated from:

$$\begin{aligned} L_{\mathrm{TR}}(\mu) &= \sum_{i=1}^{I}(g_i \ln \psi_i - \psi_i) + \alpha P(\mu) \\ \psi_i(\mu) &= n_i \exp\left(-\left(\sum_{b=1}^{J} l_{ib}\mu_b\right)\right)\sum_{j=1}^{J} c_{ij}\lambda_j = n_i a_i \sum_{j=1}^{J} c_{ij}\lambda_j \end{aligned} \tag{2.5}$$

Since attempts for developing the EM algorithm for transmission tomography have not led to an updateable expression for likelihood increment, a gradient ascent algorithm [17, 18] which directly maximizes the likelihood function can be used. L_{TR} is a complex function for direct maximization using common optimization techniques; hence it was suggested to replace it with a surrogate function that is easier to maximize (optimization transfer). The attenuation map can be updated after each iteration m (see appendix A for a detailed derivation):

$$\mu^{m+1} = \mu^m + \Delta\mu^m \tag{2.6}$$

such that [19],

$$0 = \frac{\partial L_{\mathrm{TR}}}{\partial \mu_j}(\mu^{m+1}) = \frac{\partial L_{\mathrm{TR}}}{\partial \mu_j}(\mu^m + \Delta\mu^m) = \frac{\partial L_{\mathrm{TR}}}{\partial \mu_j}(\mu^m) + \sum_h \frac{\partial^2 L_{\mathrm{TR}}}{\partial \mu_j \partial \mu_h}\Delta\mu_h^m \tag{2.7}$$

where h denotes the voxel number ($h = 1, \ldots, J$). This is satisfied by the following expression for $\Delta\mu_j^{m+1}$:

$$\Delta\mu_j^{m+1} = -\frac{\frac{\partial L_{\mathrm{TR}}}{\partial \mu_j}(\mu^m)}{\sum_h \frac{\partial^2 L_{\mathrm{TR}}}{\partial \mu_j \partial \mu_h}(\mu^m)} \tag{2.8}$$

Subsequently, the attenuation map can be rewritten as follows (detailed in appendix A)

$$\mu_j^{m+1} = \mu_j^m + \frac{\sum_{i=1}^{I} l_{ij}\psi_i^m - \left(\sum_{k=1}^{N} l_{i_k j}\frac{\psi_{i_k}^m}{\psi_{i_k}^m + \beta_{i_k}}\right) - \frac{\partial}{\partial \mu_j}(\alpha P(\mu))}{\sum_{i=1}^{I} l_{ij}\frac{(\psi_i^m)^2}{\psi_i^m + \beta_i}(\sum_{\zeta=1}^{J} l_{i\zeta}) + \sum_h \frac{\partial^2}{\partial \mu_j \partial \mu_h}(\alpha P(\mu))} \tag{2.9}$$

Where $\beta_i = \bar{s}_i + \bar{r}_i$. Because TOF information is incorporated in the activity reconstruction (eq. (2.4)), its convergence rate is higher than the attenuation map update (eq. (2.8)). To solve this issue, the cycle of attenuation updates should be done faster, such that multiple attenuation updates are performed for every activity update. Interestingly, while non-TOF reconstruction usually requires less processing time in sinogram format mode than TOF-based, list-mode based reconstruction does not have the same behavior and there is no significant difference between processing of non-TOF and TOF reconstructions in list-mode (except for the calculation of the system matrix). Fortunately, the term of $(\sum_{\zeta=1}^{J} l_{i\zeta})$ is independent of current estimations of activity and attenuation, and is only related to the number of coincidences and system matrix elements. This property allows it to be calculated once and used as a constant factor during subsequent calculations.

2023 JINST 18 P09041

2.3 Correction for random and scatter components

In order to preserve the Poisson nature of the likelihood, it is crucial to incorporate the contribution of scattering and random events during the reconstruction process itself, as opposed to prior to it. This is supported by equations (2.4) and (2.9), which clearly indicate that accounting for scattering and random events within the reconstruction framework is necessary. The random coincidences are estimated using a delayed-coincidence window method. The coincidences detected within a delayed window are counted as random coincidences for each LOR because the detection probability of a true coincidence within this window would be zero. Furthermore, the Single Scatter Simulation (SSS) algorithm was used for the estimation of the scatter component with an update for TOF-PET data [20]. The algorithm approximates the scattering component in a given LOR by single Compton scattered events only based on this assumption that the total amount of scattering can be expressed as the superposition of the contributions of many scatter points to the LOR calculated by an analytical formula. The single scatter approximation expresses the contribution of a scattering sample point S to a LOR spanned of a photon pair emitted such that one photon is detected unscattered while the other one is incident on scattering point S before reaching the detector. The expected single-scatter rate to be detected by the detector pair (A, B) is given by equation (2.10):

$$\begin{aligned}
\mathrm{SSS}(A,B) &= \int_{\text{Scattering Volume}} \left(\frac{\sigma_A \sigma_B}{4\pi R_A^2 R_B^2}\right)\left(\frac{\mu}{\sigma_c}\frac{d\sigma_c}{d\Omega}\right)(R_A + R_B)dV_s \\
R_A &= \epsilon_A(E)\epsilon_B(E')\left(e^{-\int_S^A \mu(E)dl}\right)\left(e^{-\int_S^B \mu(E')dl}\right)\left(\int_S^A F_{\mathrm{TOF}}\lambda(l)dl\right) \\
R_B &= \epsilon_A(E)\epsilon_B(E')\left(e^{-\int_S^B \mu(E)dl}\right)\left(e^{-\int_S^A \mu(E')dl}\right)\left(\int_S^B F_{\mathrm{TOF}}\lambda(l)dx\right)
\end{aligned} \tag{2.10}$$

where σ_c is the total Compton interaction cross section, Ω is the solid scattering angle, $\frac{d\sigma_c}{d\Omega}$ is the Klein-Nishina differential cross section (calculated at the angle $\angle ASB$), $E = 511\,\mathrm{keV}$ and E' is scattered energy. Furthermore, let σ_A and σ_B denote the geometrical cross section of detector A and B for rays incident along AS (detector A to sample scattering point S) and SB (detector B to sample scattering point S), R_A and R_B are the distances between the sample point and detectors A and B, respectively. A simple model of the detector efficiencies, contingent upon the photon energy, energy resolution and discriminator bounds of detectors is provided by ϵ_A and ϵ_B. F_{TOF} incorporates TOF information using modeling with a quasi-Gaussian function based on the TOF value and effective TOF resolution of the system [20, 21].However, this technique requires the actual attenuation map and corrected emission images, yet reconstruction without accurate scatter estimation does not provide quantitative images. To solve this problem, an iterative approach was utilized, such that the estimation of the scatter component is updated for current estimation of attenuation and activity images. This means that at each iteration of the reconstruction process, a new scattering component is computed, taking into account the most up-to-date activity and attenuation estimations. This updated scattering component is then utilized in the subsequent iteration of the reconstruction, contributing to the refinement of both the activity and attenuation maps. Due to the computational cost, our implementation of SSS-TOF has been slightly modified through the use of a coarse grid

2023 JINST 18 P09041

sampling of scattering points where scatter estimation is interpolated from this grid to physical LOR space to operate directly in list-mode iterative reconstruction. The suggested algorithm employs the attenuation map for the purpose of excluding regions that fall outside the patient's designated area. For each point of scattering coarse grid, the scattering expected ratio for each detector pair is estimated and then summed over all scatter points (eq. (2.11)). Finally the scattering component is modeled by scaling as an integral transformation of the single scatter distribution.

2.4 Algorithm implementation and image quality assessment

The proposed algorithm was implemented with and without a smoothness prior. A Median root prior (MRP) [22] was used as penalty using a Maximum a Posterior (MAP) framework that can be weighted by the Bayesian parameter α. The prior objective function of MRP can be defined as follows:

$$P(\mu) = -\sum_{j=1}^{J} \frac{(\mu_j - m_j)^2}{2m_j} \tag{2.11}$$

where m_j denotes the median of voxels in the neighbourhood centred at j. In this study, α is chosen based on visual inspection through trial and error to produce a uniform attenuation map. Because the attenuation map derived by MLAA is biased with an unknown constant [8], the peak shifting method was used to solve the scaling problem [23]. In this method, to mitigate potential bias resulting from an incorrect scaling factor, the estimated attenuation maps were rescaled during each iteration. The rescaling aimed to align the most frequent attenuation coefficient in the histogram with the dominant actual attenuation coefficient in the object, which was set to 0.096 cm^{-1} for water. This adjustment ensured that the estimated attenuation maps accurately represent the expected attenuation properties of the object, minimizing any scaling-related biases.

List-mode image reconstruction has a high computational cost owing to a large amount of data, and as such, there is a demand to reduce the computational time for each event. With use of an on-the-fly approach for calculation of system matrix, the elements of the system matrix are calculated during the reconstruction process rather than pre-calculating and storing them on a hard disk (as a lookup table), which is often used in histogram-based reconstructions. In the current study, an approach based on the volume of the intersection computation method was used [24]. In this approach, cubic image voxels and rectangular Tubes of Response (ToRs) in 3D PET are approximated using spheres and cylinders, respectively, to account for the finite size of the crystals and provide a realistic model of the physical system. The advantage of this modelling is that the relative orientation of voxels and ToRs is neglected and the volume of intersection between a voxel and the ToR is calculated based on the distance between the voxel center and ToR axis. A normal probability density function was incorporated in the system matrix calculation step to account for TOF information. This method allows rapid on-the-fly computation of the system matrix and hence reduces its computational complexity in LM-MLAA. The intersection volume of the modelled spheres with TOR cylinder calculated using an analytical expression based on the elliptic integrals provides a significant reduction of the time-consuming system matrix extraction process while keeping the same accuracy.

Since emission-based methods are not able to estimate attenuation coefficients for LORs that do not intersect non-zero activity distributions, a background mask was obtained from a few iterations

2023 JINST 18 P09041

of activity map reconstruction without attenuation correction to estimate the contour of the scanned object. Based on this mask, attenuation coefficients estimation was confined to regions of the attenuation map with activity support. The initial attenuation map was made by filling the background mask uniformly with the water attenuation coefficient. The activity images reconstructed using the original attenuation map at different TOF resolutions were used as reference activity maps (MLEM). For evaluation of the contrast and noise properties of the reconstructed activity images, the contrast recovery coefficient (CRC) and relative standard deviation (RSD) were used. The $\mathrm{CRC_{hot}}$ for each hot source was defined as:

$$\mathrm{CRC_{hot}} = \frac{\frac{H_s}{B} - 1}{R_{\mathrm{HB}} - 1} \tag{2.12}$$

where H_s is the average activity concentration of each hot source, B denotes the background activity concentration and R_{HB} is the hot to background ratio. Also, $\mathrm{CRC_{cold}}$ for each cold region was defined as:

$$\mathrm{CRC_{cold}} = 1 - \frac{C_s}{B} \tag{2.13}$$

where C_s represents the average activity concentration of each cold region. To analyze the CRC for both hot and cold sources, the initial step involved generating a mask image that assigned distinct tags to each source (hot and cold) and included a designated region for the background. This mask facilitated the extraction of corresponding voxels from the reconstructed activity and attenuation maps for each specific region. Subsequently, the mean and standard deviation of the intensities of extracted voxels were computed for each region. Notably, the background region was defined as a cylindrical region situated at the center of the phantom, devoid of any hot or cold sources. The diameter of this background region was twice the size of the largest source, measuring 50 mm.

2.5 Monte Carlo simulation studies

The performance of the proposed method was evaluated using simulated TOF PET data obtained using GATE Monte Carlo package [25]. The PET system geometry corresponded to the GE Discovery-690TOF PET/CT scanner using 13,824 LYSO crystals arranged on 24 rings with crystal dimensions of $4.2 \times 6.3 \times 25\ \mathrm{mm}^3$. The transaxial FOV and coincidence time windows are 700 mm and 4.9 ns, respectively [26]. TOF resolutions of 100, 300, and 544 ps were modelled to evaluate the effect of image quality in the absence of noise and dead-time. A Monte Carlo simulation was conducted to generate list-mode data of a ACR[1] phantom. This cylindrical phantom features a fillable design with an internal radius of 10.8 cm and a height of 10 cm. It includes seven thin-walled cylinders consisting of four fillable tubes with diameters of 8, 12, 16, and 25 mm, as well as other cold solid rods with a diameter of 25 mm. The fillable tubes were filled with air, water, and Teflon having linear attenuation coefficients of 1.116×10^{-4}, 0.0961 and $0.1813\ \mathrm{cm}^{-1}$, respectively.The background compartment (5,700 ml) was filled with 4.5 kBq/ml ^{18}F solution, whereas the fillable tubes were filled with nine kBq/ml activity concentration resulting in a source-to-background ratio of 2. In addition, another experiment was performed with a source-to-background ratio of 4 to evaluate the impact on reconstructed images.The output of simulation was post-processed using an in-house software to generate list-mode files. During the simulation, the following parameters were utilized: an energy resolution of 12.5%, an energy window ranging from 425 to 650 keV, and a data acquisition duration of 600 seconds. The reconstruction process involved 20 iterations, reconstructing images

2023 JINST 18 P09041

with a size of $256 \times 256 \times 47$ (voxel size: $2.73 \times 2.73 \times 3.27\,\mathrm{mm}^3$), without applying any smoothing filters. In the proposed approach implementation, five attenuation updates were performed for every activity update. Additionally, it should be mentioned that, during the first three iterations, the scattering calculation step was turned off to obtain initial estimations of the activity and attenuation maps. For the scattering calculation, mesh dimensions of 0.7 cm transversely and 0.7 cm axially were employed, resulting in approximately 180k sampling points across the entire FOV with a low energy threshold of 425 keV as a discriminator. In order to improve calculation speed and reduce the number of sampling points, a rejection step was implemented. During this step, points were rejected if the attenuation coefficient associated with their location was below a certain threshold ($0.02\,\mathrm{cm}^{-1}$). It is worth noting that the simulation's accuracy exhibits minimal sensitivity to the grid size, whereas the computational time varies inversely with the product of the three mesh dimensions. The scaling factor is calculated by performing tail-fitting in the scatter-only region, which exists outside the object. To identify this region, the current estimation of the activity and attenuation map is forward projected and masked accordingly. Within this masked region, the scatter estimate is then time-integrated, interpolated, and subjected to a least-squares affine fitting procedure.

3 Results

The actual attenuation and emission maps along with MLEM reconstructions of PET emission images with a known attenuation map and reconstructed attenuation and activity maps using the proposed method at different TOF resolutions are depicted in figure 1. The reconstructed activity map obtained with MLEM method using a known attenuation map is considered as the gold standard data. This serves as the reference against which other methods are compared. The MLEM method with a known attenuation map corresponds to the scenario commonly encountered in PET/CT imaging, where the attenuation map is derived from the CT image and then used for reconstructing the activity map. However, visually discerning differences between MLEM images, particularly between reconstructions with TOF resolutions of 300 and 544 ps, can be challenging. In such cases, focusing the observation on the better recovery of the hot source regions can be beneficial. With a TOF resolution of 300 ps, the largest hot source exhibits improved uniformity, and the presence of the smallest hot source is clearly discernible. Table 1 provide a statistical compression between reconstructed images and actual ones at different TOF resolutions.

Table 1. Comparison of the reconstructed activity and attenuation maps for the ACR phantom using the proposed method and actual images with metrics of MSE, SNR, PSNR, and CC. Actual attenuation image and MLEM reconstructed activity maps using actual attenuation map at different time resolutions were used as reference images.

Scanner time resolution	**Activity**				**Attenuation**			
	MSE	**PSNR**	**SNR**	**CC**	**MSE**	**PSNR**	**SNR**	**CC**
100 ps	0.0028	25.57	27.33	0.9996	1.05×10^{-7}	69.78	16.95	0.9899
300 ps	0.0082	20.89	22.65	0.9976	1.65×10^{-7}	67.83	14.99	0.9842
544 ps	0.0931	10.31	12.07	0.9838	3.35×10^{-7}	64.75	11.91	0.9752

2023 JINST 18 P09041

Table 2. Relative error (%) in the mean estimated attenuation coefficients after 20 and 50 iterations at different coincidence time resolutions.

	20 iterations			50 iterations		
Scanner Time Resolution	**ROI 1 (Air)**	**ROI 2 (Water)**	**ROI 3 (Teflon)**	**ROI 1 (Air)**	**ROI 2 (Water)**	**ROI 3 (Teflon)**
100 ps	383.74	4.50	−14.23	309.99	5.72	−8.28
300 ps	443.87	6.80	−15.37	333.93	5.45	−9.80
544 ps	534.48	12.31	−14.17	334.08	1.85	−13.74

A sense of the attenuation reconstruction quality using the proposed technique with and without MRP is shown in the profile plots of figure 2. It can be observed that LM-MLAA and LM-MLAA-MRP overestimate the attenuation coefficients for the air region. This causes the activity profiles in this area to be more intense than actual values (figure 3). While LM-MLAA-MRP improves image uniformity especially, in the background, owing to the presence of a smoothing term, the estimated attenuation coefficients are lower than the default LM-MLAA.

Figure 4 shows the mean and standard deviation of the estimated attenuation coefficients at each iteration of the LM-MLAA method for cold regions of the ACR phantom. The actual attenuation coefficients for each class are shown by horizontal red solid lines. Table 2 shows the error on the mean estimated attenuation coefficients after 20 and 50 iterations at different TOF resolutions. It should be noted that the actual attenuation coefficient of the air region is very low ($1.116e^{-4}\,cm^{-1}$), and hence the relative errors for this region appear high. The presented algorithm estimates reasonably well attenuation for water class with a reasonable standard deviation, while it underestimates the mean attenuation coefficients for air and Teflon classes. Moreover, it should be emphasized that with improving the TOF resolution, the underestimation is reduced especially for air region.

Figure 5 and 6 depict CRC vs. RSD trade-off performance curves (generated with increasing iterations) for hot sources with different hot to background ratios and cold sources at different TOF resolutions, respectively. The LM-MLAA method managed well the effect of the change of the different source to background ratios showing considerable similarity in the behaviour of CRC curves for LM-MLAA and standard MLEM at different TOF resolutions. In addition, one can observe that, for LM-MLAA reconstruction, the effect of improved TOF resolution is greater on the larger hot sources.

4 Discussion

In the present work, a list-mode emission-based maximum likelihood reconstruction of attenuation and activity approach has been presented for TOF-PET. List-mode processing is an invaluable approach that guarantees the incorporation of all available information during the reconstruction process. By utilizing list-mode data, the reconstruction algorithm can leverage the detailed information from each individual event, resulting in a more comprehensive and accurate reconstruction. This enables the preservation of fine temporal details and the extraction of maximum information from the acquired data (dynamics of the acquisition). However, it is crucial to acknowledge the trade-offs that accompany list-mode processing, particularly in relation to computational costs. The proposed method uses a fast and precise on-the-fly system matrix computation and an optimized SSS algorithm

2023 JINST 18 P09041

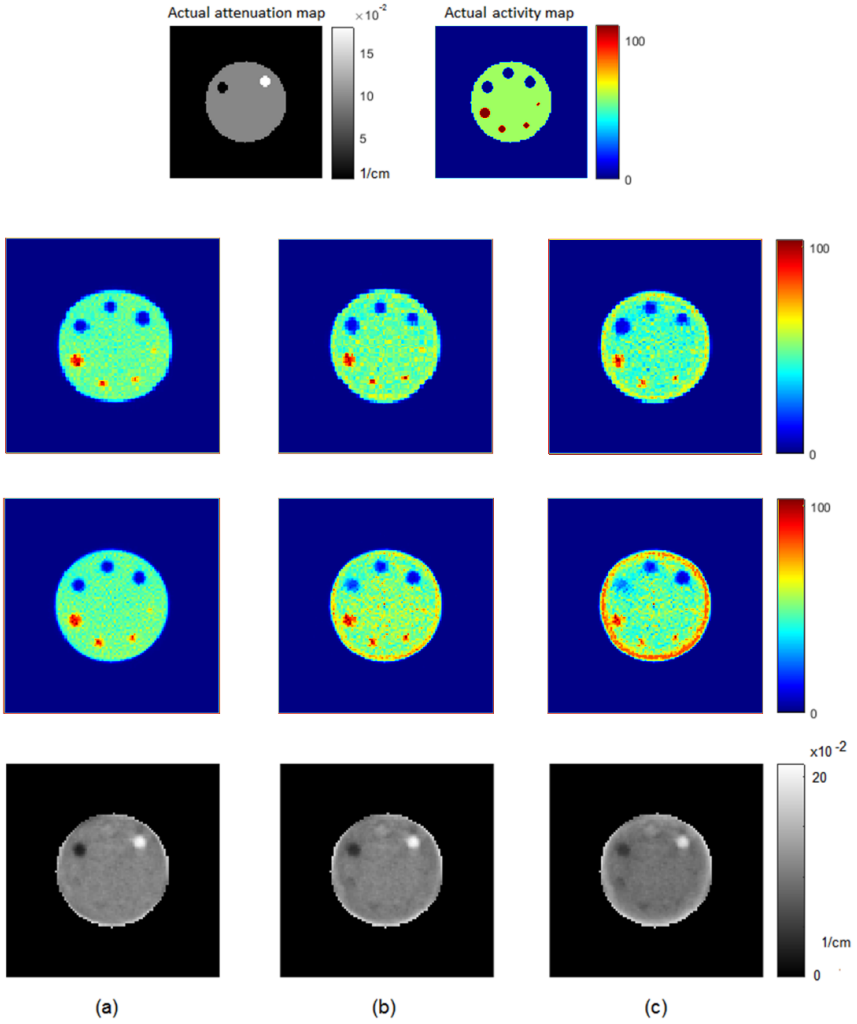

Figure 1. First row: actual attenuation and activity distributions. Second row: MLEM reconstructed images with known attenuation map. Third row: activity reconstructed images using LM-MLAA, Forth row: attenuation reconstructed images using LM-MLAA. The columns represent various TOF resolutions, namely: (a) 100 ps, (b) 300 ps, and (c) 544 ps.

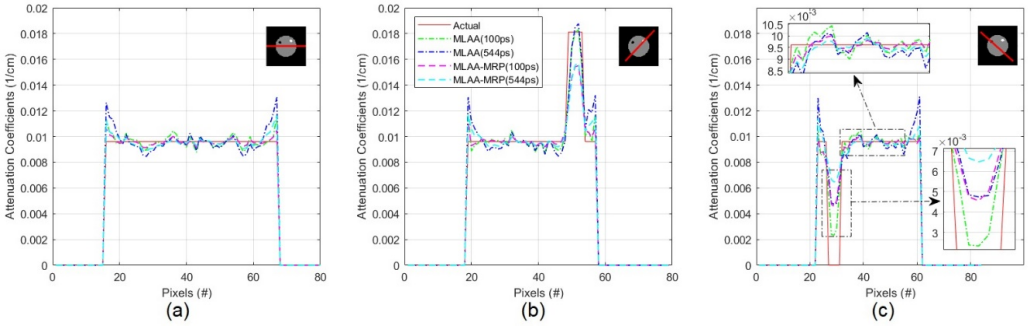

Figure 2. Comparison of attenuation map profiles for the ACR phantom with and without MRP at TOF resolutions of 100 ps and 544 ps, in comparison to the ground truth profiles.

2023 JINST 18 P09041

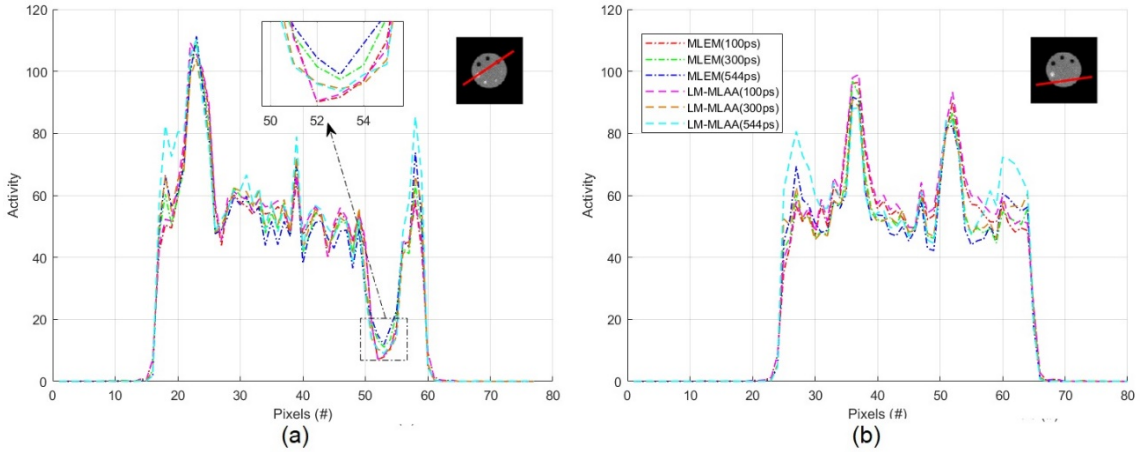

Figure 3. Profiles of the reconstructed activity maps for list-mode MLAA compared to the MLEM reconstructed images with known attenuation maps at time resolutions of 100 ps, 300 ps and 544 ps.

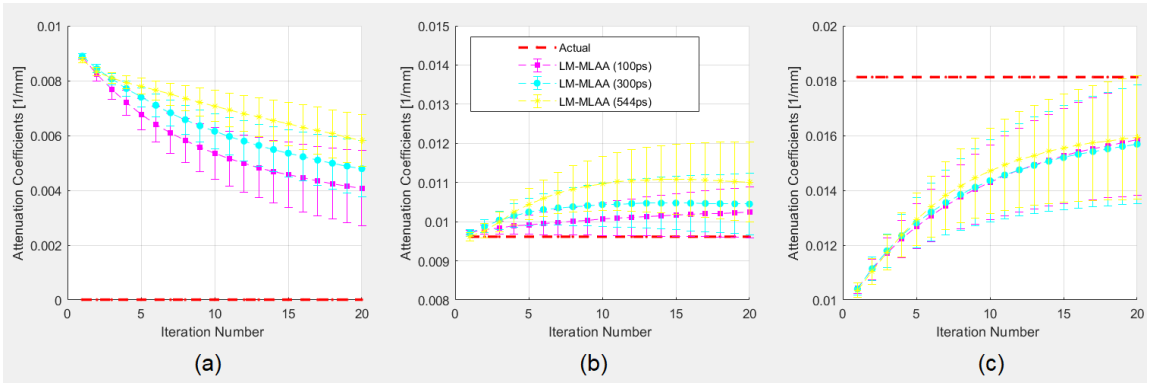

Figure 4. Estimated attenuation coefficients by the proposed method at different reconstruction iteration numbers in (a) Air, (b) Water, and (c) Teflon Regions. The dot points represent the mean of the estimated attenuation coefficients, while the error bars depict the ± one standard deviation.

for compensation of scattering coincidences to implement joint list mode reconstruction. The evaluation shows that the system TOF resolution and initial attenuation map have significant effects on the image quality of images reconstructed using LM-MLAA (figures 3 and 4), especially for large objects. Prior to the introduction of silicon photomultiplier (SiPM)-based TOF PET, the TOF resolution of most state-of-the-art clinical TOF-PET scanners were in the range of 500–600 ps. Recent progress in the field of PET instrumentation, including fast detectors and readout electronics, is expected to pave the way for the development of next-generation TOF-PET scanners [27, 28] in order to remove the barriers for clinical application of LM-MLAA.

One of the drawbacks of LM-MLAA is that the estimated attenuation coefficients from the emission data for regions outside the activity support are inaccurate, even in the absence of noise. In addition, it produces less accurate attenuation coefficients for regions with very limited tracer uptake, e.g. near the boundaries of objects whose LORs have vanishing activity as one approaches the boundary. Hence, a background mask or penalty could be used to set to zero the attenuation

2023 JINST 18 P09041

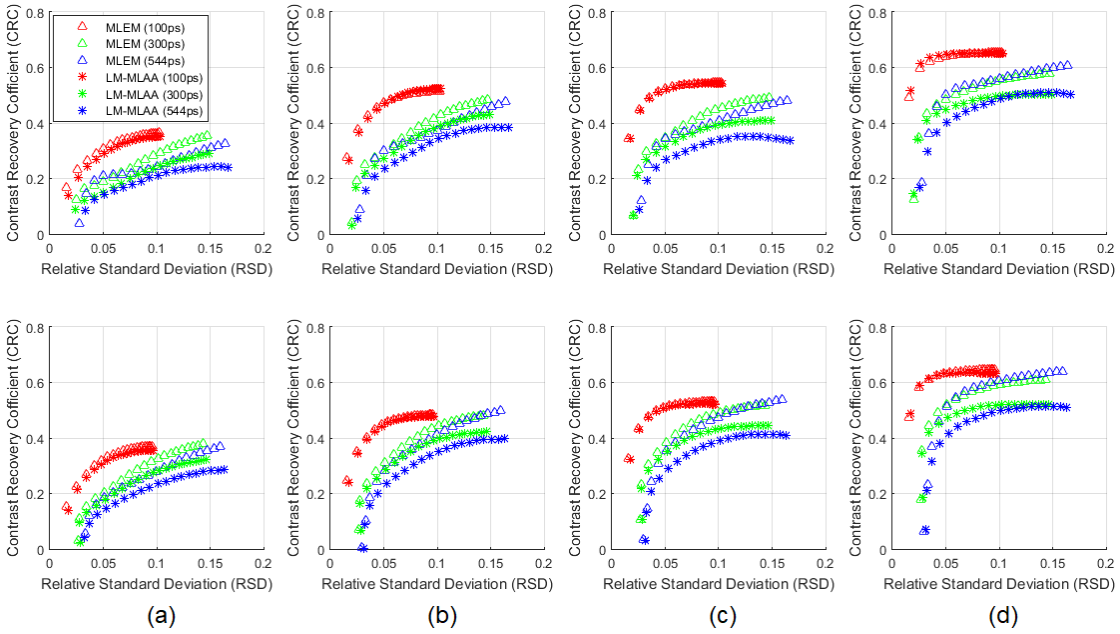

Figure 5. Contrast (CRC) versus noise (RSD) for hot sources in the ACR phantom on ROI regions with diameters of (a) 8, (b) 12, (c) 16 and (d) 25 mm at different iteration numbers. Noise was computed in a ROI located in the centre of image with diameter of 50 mm. Top row shows results for a source-to-background contrast ratio of 2 while the last row shows the same results for source-to-background ratio of 4.

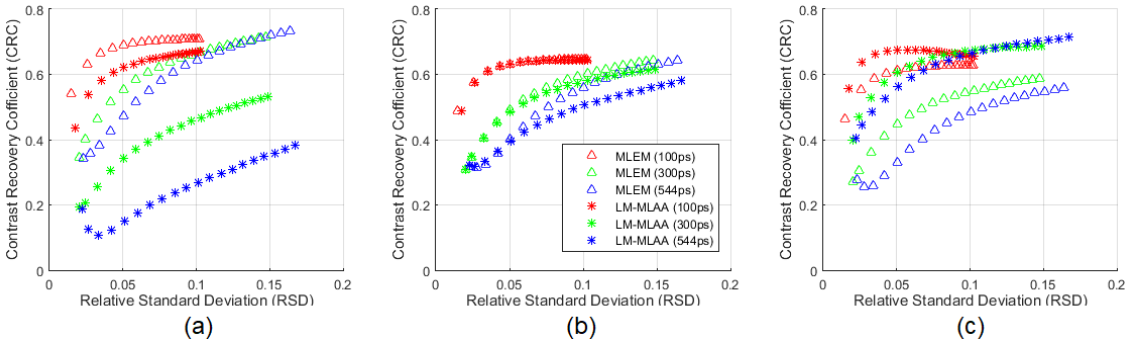

Figure 6. Contrast (CRC) versus noise (RSD) for cold sources in the ACR phantom on (a) air, (b) water and (c) Teflon regions at different iteration numbers which shown using markers.

coefficients in regions of no or with very limited tracer uptake. In studies where the attenuation map includes areas outside the contour of activity distribution (such as scanner bed, coils, etc.), the use of complementary information is necessary to complete the attenuation map [3].

The standard emission-based method for joint reconstruction of activity and attenuation maps often suffers from noise due to the limited counting statistics of PET emission data. The utilization of TOF data effectively eliminates high-frequency cross-talk in joint estimation problem [29], with the extent of cross-talk reduction being dependent on the TOF resolution value (figure 1). However, to address low-frequency cross-talk, it is beneficial to incorporate prior knowledge about the activity and/or the attenuation map into the reconstruction process, thereby confining the maximization of

2023 JINST 18 P09041

the log-likelihood function. In addition to suppressing low-frequency cross-talk, the incorporation of prior knowledge such as anatomical priors and/or histogram-based information [2, 30] in the reconstruction process also accelerates the identification of optima and is necessary to bind the scaled solutions. Incorporating a smoothness prior (LM-MLAA-MRP) to the attenuation map derivation process can reduce the RSD, thus resulting in a higher uniformity in the attenuation map. However, this might blur the edges, reduce the attenuation map contrast and result in less accurate attenuation coefficients.

Figure 4 illustrates the attempt of the proposed approach to approximate the actual values of attenuation coefficients. However, depending on the TOF resolution, a bias may exist, making it difficult to achieve the exact values even with a high number of iterations. In such situations, the selection of the starting point, particularly the initial attenuation map, becomes crucial. In this specific study, we initiated the reconstruction process from scratch without an appropriate initial attenuation map and did not incorporate any prior information (except the smoothing term) to constrain the solution throughout the iterations. It seems that LM-MLAA initiated and confined by MRI could be a robust and reliable approach for attenuation map derivation in hybrid PET/MRI [3].

The weighting factor of the smoothing prior (α) is currently determined through visual inspection, which may lead to a count/tracer-dependent output. Selecting very large values for it can result in a smoothed attenuation image and delay the estimation of the attention map and hence necessitates the use of more iterations for reconstruction. Therefore, it is preferred to choose a lower value for it, as it allows for obtaining more detailed attenuation maps. However, using a low value may introduce artifacts in the activity images due to the lack of uniformity across different regions of the attenuation maps. To address this limitation and prevent excessive suppression of details in the reconstructed image, a dynamic parameter can be employed. By starting with a low value for this factor and gradually increasing it during the iteration process, a more creative approach can be adopted to achieve an optimal balance between preserving image details and achieving desired smoothing effects.

Unlike the histogramming mode, LM-MLAA computation time strongly depends on the number of measured coincidences. The use of the developed system matrix calculation method allows rapid on-the-fly computation of the volume of intersection between LORs and voxels. Future work should focus on ascertaining the level of accuracy needed for the sensitivity matrix calculation and performing clinical studies to thoroughly assess the performance of LM-MLAA method in the different clinical setting.

5 Conclusions

We developed and assessed a novel list-mode based algorithm for joint estimation of activity and attenuation maps from emission data in TOF-PET imaging. The technique was evaluated extensively using Monte Carlo simulated studies at different TOF resolutions. The approach looks promising for deriving patient-specific attenuation maps and is reasonably robust to errors that can lead to an improvement in image quality. The proposed method may open new perspectives for PET imaging applications that do not allow the use of transmission scanning to derive the attenuation map, such as PET, PET/MRI, PET/CT studies with a reduced CT field-of-view or applications where patient motion prevents direct utilization of CT data.

2023 JINST 18 P09041

Acknowledgments

This work was supported by Iran National Science Foundation (INSF) grant no. 97010825, Tehran University of Medical Sciences under grant no. 36950 and the Swiss National Science Foundation under grant SNFN 320030_176052.

A Joint reconstruction of activity and attenuation maps in list mode

In TOF PET, the mean number of detected coincidences for LOR i with associated detection photon time difference t, $\overline{g}_{it}$, is expressed as:

$$\overline{g}_{it} = n_i e^{-\sum_k l_{ik}\mu_k} \sum_{j=1}^{J} c_{ijt}\lambda_j + \overline{S}_{it} + \overline{r}_{it} \tag{A.1}$$

where λ and μ are the activity and attenuation vectors, respectively, n_i is a normalization factor, the term $e^{-\sum_k l_{ik}\mu_k}$ models photon attenuation, c_{ijt} represent the coefficients of the system matrix (scanner geometry and physical imaging processes) for LOR i, voxel j and TOF bin t, and $\overline{S}_{it}$ and $\overline{r}_{it}$ denote the estimated scattered and random coincidences for the LOR i at TOF bin t. In addition, J represents the number of voxels in the activity map, and l_{ik} denotes the attenuation intersection length for LOR i and voxel k. The activity and attenuation maps can be determined from the measured PET emission data g_{it} using the log-likelihood maximization:

$$\begin{aligned} L(g|(\lambda,\mu)) &= \sum_{it} g_{it} \ln \overline{g}_{it} - \overline{g}_{it} \\ \hat{\lambda},\hat{\mu} &= \arg\max_{\lambda,\mu}\{L(g|\lambda,\mu) + \alpha P(\mu)\} \end{aligned} \tag{A.2}$$

where L and P denote the objective function corresponding to the logarithm of the likelihood and prior terms for the attenuation map. Please note that when calculating the activity map in PET, it is important to take into account the time information. However, it is worth emphasizing that the attenuation map does not depend on the time index. This is because the attenuation coefficient specifically reflects the extent of photon absorption or scattering as they propagate through the body tissue, and this physical property remains constant regardless of the time frame being considered. In other words, the attenuation length remains unaffected by the time index, meaning that photons originating from different locations along a LOR will experience the same attenuation coefficient. The attenuation along each LOR i can be described as:

$$a_i^m = \exp\left(-\left(\sum_{b=1}^{J} l_{ib}\mu_b^m\right)\right) \tag{A.3}$$

where m is the iteration number.

A.1 Activity update

The list-mode algorithm for activity reconstruction can be formulated as follows:

$$\lambda_j^{m+1} = \frac{\lambda_j^m}{\sum_{i=1}^{I} n_i a_i^m c_{ijt}} \left(\sum_{k=1}^{N} n_{i_k} a_{i_k}^m c_{i_k jt} \frac{1}{(n_{i_k} a_{i_k}^m \sum_{b=1}^{J} c_{i_k bt}\lambda_b^m) + \overline{s}_{i_k t} + \overline{r}_{i_k}}\right) \tag{A.4}$$

2023 JINST 18 P09041

where i_k is the corresponding LOR of the k^{th} list-mode event, N is the total number of measured events, I denotes the total number of possible LORs.

A.2 Attenuation update

A.2.1 Maximum likelihood gradient ascent optimization

Maximizing the likelihood directly (at fixed activity) by setting its partial derivatives to μ_j to zero is not feasible. The resulting set of equations depend nonlinearly on the unknowns μ and the set of equations are coupled through μ. Since attempts for developing the EM algorithm for transmission tomography have not led to an updateable expression for likelihood increment, a gradient ascent algorithm [17, 18] which directly maximizes the likelihood function can be used. The attenuation map can be updated after each iteration m:

$$\mu^{m+1} = \mu^m + \Delta\mu^m \tag{A.5}$$

The proposed solution by Nuyts et al. [17] involves approximating the likelihood through a Taylor series expansion cantered around the current guess (λ^k, μ^k). This approximation is based on the quadratic terms and truncates higher-order terms. Furthermore, to simplify the expression, the quadratic terms in μ are decoupled. This simplification leads to the development of the Maximum Likelihood for Transmission (MLTR) algorithm as the resulting update [17, 19].

The Taylor Expansion of a real valued differentiable function $f : \omega \to \mathbb{R}$ around x and truncated at the second order term, is given by

$$f(x + \delta x) = f(x) + (\delta x)^T \nabla f(x) + \frac{1}{2}(\delta x)^T \nabla^2 f(\overline{x})(\delta x) \tag{A.6}$$

where ∇^k is the kth directional derivative in the direction of δx and $\overline{x}$ is somewhere on the line segment connecting x with $x + \delta x : \overline{x} = x + \tau\delta x, \tau \in [0, 1]$.

Based on this expansion for the likelihood around the current guess μ^m:

$$L(\mu, \hat{\lambda}^m; g) \approx L(\hat{\mu}^m, \hat{\lambda}^m; g) + \sum_j \frac{\partial L}{\partial \mu_j}|_{\mu^m} \Delta\mu_j + \frac{1}{2} \sum_{jh} \frac{\partial^2 L}{\partial \mu_j \partial \mu_h}|_{\mu^m} \Delta\mu_j \Delta\mu_h \tag{A.7}$$

Where $\Delta\mu_j = \mu_j - \hat{\mu}_j^k$. Since

$$0 \leq (\Delta\mu_j - \Delta\mu_{j'})^2 \Rightarrow 2\Delta\mu_j \Delta\mu_{j'} \leq \Delta\mu_j^2 + \Delta\mu_{j'}^2 \tag{A.8}$$

Since the second derivatives are all negative (Assuming this condition also holds if the background is not too large)

$$\frac{1}{2} \sum_{jh} \frac{\partial^2 L}{\partial \mu_j \partial \mu_h}|_{\mu^m} \Delta\mu_j \Delta\mu_{j'} \geq \frac{1}{4} \sum_{jh} \frac{\partial^2 L}{\partial \mu_j \partial \mu_h}|_{\mu^m} (\Delta\mu_j^2 + \Delta\mu_h^2) = \frac{1}{2} \sum_{jh} \frac{\partial^2 L}{\partial \mu_j \partial \mu_h}|_{\mu^m} \Delta\mu_j^2 \tag{A.9}$$

Filling this in into equation (A.7), a surrogate function is constructed which is equal to in the current solution and smaller than elsewhere.

$$L(\mu, \hat{\lambda}^m; g) \gtrsim L(\hat{\mu}^m, \hat{\lambda}^m; g) + \sum_j \frac{\partial L}{\partial \mu_j} . \Delta\mu_j + \frac{1}{2} \sum_{jh} \frac{\partial^2 L}{\partial \mu_j \partial \mu_h}|_{\mu^k} \Delta\mu_j^2 \tag{A.10}$$

2023 JINST 18 P09041

As a result, the quadratic terms are uncoupled in $\Delta\mu$. By maximizing the surrogate function (setting the derivatives to $\mu_j : j = 1, \ldots, J$; $j = 1$ of the right hand side of (A.10) to zero), gives:

$$\Delta\mu_j^{m+1} = -\frac{\cdot \frac{\partial L}{\partial \mu_j}|_{\mu^m}}{\sum_h \cdot \frac{\partial^2 L}{\partial \mu_j \partial \mu_h}|_{\mu^m}} \tag{A.11}$$

This update maximizes surrogate function which guarantees an increase of (A.7).

A.2.2 Calculations of derivatives of likelihood

Considering the Poisson likelihood in equation (A.2), for simplicity in writing, let's define the following variables:

$$\begin{aligned} \overline{g}_{it} &= \overline{\psi_{it}} + \beta_{it} \\ \overline{\psi_{it}} &= n_i a_i p_{it} \\ p_{it} &= \sum_{j=1}^{J} c_{ijt} \lambda_j \end{aligned} \tag{A.12}$$

where β_{it} is the expectation value of the background and $\overline{\psi_{it}}$ is the expectation value of the trues with n_i the sensitivity of LOR i and p_{it} the projected activity without taking the attenuation nor the sensitivity into account. The first and second derivatives of the likelihood can be defined as:

$$\begin{aligned} \frac{\partial L}{\partial \lambda_j} &= \sum_{it} \frac{n_i a_i c_{ijt}}{\overline{g}_{it}} (g_{it} - \overline{g}_{it}) \\ \frac{\partial L}{\partial \mu_j} &= -\sum_{it} l_{ij} \frac{\overline{\psi_{it}}}{\overline{g}_{it}} (g_{it} - \overline{g}_{it}) \\ \frac{\partial^2 L}{\partial \lambda_j \partial \lambda_{j'}} &= -\sum_{it} g_{it} \frac{(n_i a_i c_{ijt})(n_i a_i c_{ij't})}{\overline{g}_{it}^{\,2}} \\ \frac{\partial^2 L}{\partial \mu_j \partial \mu_h} &= -\sum_{it} (l_{ij} l_{ih}) \overline{g}_{it} \left[1 - \frac{g_{it}}{\overline{g}_{it}} \frac{\beta_{it}}{\overline{g}_{it}} \right] \\ \frac{\partial^2 L}{\partial \lambda_j \partial \mu_h} &= \sum_{it} (l_{ih} n_i a_i c_{ijt}) \left[1 - \frac{g_{it}}{\overline{g}_{it}} \frac{\beta_{it}}{\overline{g}_{it}} \right] \end{aligned} \tag{A.13}$$

Furthermore, when $\beta = 0$, we can express the simplified versions.

$$\begin{aligned} \frac{\partial L}{\partial \mu_j} &= -\sum_{i} l_{ij} (g_{it} - \overline{g}_{it}) \\ \frac{\partial^2 L}{\partial \mu_j \partial \mu_h} &= -\sum_{i} (l_{ij} l_{ih}) \overline{g}_{it} \\ \frac{\partial^2 L}{\partial \lambda_j \partial \mu_h} &= \sum_{i} (l_{ih} n_i a_i c_{ijt}) \end{aligned} \tag{A.14}$$

2023 JINST 18 P09041

A.2.3 Transmission model with prior

The log-likelihood for transmission tomography keeping λ constant can be calculated from:

$$\begin{aligned} L_{TR}(\mu) &= \sum_{i=1}^{I}(g_i \ln \psi_i - \psi_i) + \alpha P(\mu) \\ \psi_i(\mu) &= n_i \exp\left(-\left(\sum_{b=1}^{J} l_{ib}\mu_b\right)\right)\sum_{j=1}^{J} c_{ij}\lambda_j = n_i a_i \sum_{j=1}^{J} c_{ij}\lambda_j \end{aligned} \tag{A.15}$$

As the summation exists between two terms, we can separate the calculation of the deviations and then perform the final summation. Based on the equation (A.11) for $\Delta\mu_j^{m+1}$ and derivatives of likelihood (equation (A.13)), the attenuation map can be rewritten as follows:

$$\mu_j^{m+1} = \mu_j^m + \frac{\sum_{i=1}^{I} l_{ij}\frac{\psi_i^m}{\psi_i^m+\beta_i}(\psi_i^m + \beta_i - g_i) - \frac{\partial}{\partial\mu_j}(\alpha P(\mu))}{\sum_{i=1}^{I} l_{ij}\frac{(\psi_i^m)^2}{\psi_i^m+\beta_i}(\sum_{\zeta=1}^{J} l_{i\zeta}) + \sum_h \frac{\partial^2}{\partial\mu_j\partial\mu_h}(\alpha P(\mu))} \tag{A.16}$$

Where $\beta_i = \overline{s}_i + \overline{r}_i$. Finally, the attenuation update equation in list mode can be expressed as follows:

$$\mu_j^{m+1} = \mu_j^m + \frac{\sum_{i=1}^{I} l_{ij}\psi_i^m - (\sum_{k=1}^{N} l_{i_k j}\frac{\psi_{i_k}^m}{\psi_{i_k}^m+\beta_{i_k}}) - \frac{\partial}{\partial\mu_j}(\alpha P(\mu))}{\sum_{i=1}^{I} l_{ij}\frac{(\psi_i^m)^2}{\psi_i^m+\beta_i}(\sum_{\zeta=1}^{J} l_{i\zeta}) + \sum_h \frac{\partial^2}{\partial\mu_j\partial\mu_h}(\alpha P(\mu))} \tag{A.17}$$

References

[1] H. Zaidi and B. Hasegawa, *Determination of the attenuation map in emission tomography*, *J. Nucl. Med.* **44** (2003) 291.

[2] Y. Berker and Y. Li, *Attenuation correction in emission tomography using the emission data — A review*, *Med. Phys.* **43** (2016) 807.

[3] V. Keereman et al., *Challenges and current methods for attenuation correction in PET/MR*, *Magn. Reson. Mater. Phys. Biol. Med.* **26** (2012) 81.

[4] A. Mehranian and H. Zaidi, *Joint Estimation of Activity and Attenuation in Whole-Body TOF PET/MRI Using Constrained Gaussian Mixture Models*, *IEEE Trans. Med. Imag.* **34** (2015) 1808.

[5] J. Nuyts et al., *Simultaneous maximum a posteriori reconstruction of attenuation and activity distributions from emission sinograms*, *IEEE Trans. Med. Imag.* **18** (1999) 393.

[6] M. Conti, *Why is TOF PET reconstruction a more robust method in the presence of inconsistent data?*, *Phys. Med. Biol.* **56** (2010) 155.

[7] A. Mehranian and H. Zaidi, *Impact of Time-of-Flight PET on Quantification Errors in MR Imaging-Based Attenuation Correction*, *J. Nucl. Med.* **56** (2015) 635.

[8] M. Defrise, A. Rezaei and J. Nuyts, *Time-of-flight PET data determine the attenuation sinogram up to a constant*, *Phys. Med. Biol.* **57** (2012) 885.

[9] A. Salomon et al., *Simultaneous Reconstruction of Activity and Attenuation for PET/MR*, *IEEE Trans. Med. Imag.* **30** (2011) 804.

[10] H. Hemmati, A. Kamali-Asl, P. Ghafarian and M.R. Ay, *Reconstruction/segmentation of attenuation map in TOF-PET based on mixture models*, *Ann. Nucl. Med.* **32** (2018) 474.

2023 JINST 18 P09041

[11] Y. Berker, F. Kiessling and V. Schulz, *Scattered PET data for attenuation-map reconstruction in PET/MRI*, *Med. Phys.* **41** (2014) 102502.

[12] H. Hemmati, A. Kamali-Asl, M. Ay and P. Ghafarian, *Compton scatter tomography in TOF-PET*, *Phys. Med. Biol.* **62** (2017) 7641.

[13] A. Rahmim et al., *Statistical list-mode image reconstruction for the high resolution research tomograph*, *Phys. Med. Biol.* **49** (2004) 4239.

[14] A. Rahmim et al., *Statistical dynamic image reconstruction in state-of-the-art high-resolution PET*, *Phys. Med. Biol.* **50** (2005) 4887.

[15] A. Rezaei, M. Bickell, R. Fulton and J. Nuyts, *Joint activity and attenuation reconstruction of listmode TOF-PET data*, in the proceedings of the *IEEE Nuclear Science Symposium and Medical Imaging Conference*, San Diego, CA, U.S.A., 31 October–7 November 2015 [DOI:10.1109/nssmic.2015.7582250].

[16] A.J. Reader, *List-mode EM algorithms for limited precision high-resolution PET image reconstruction*, *Int. J. Imag. Syst. Technol.* **14** (2004) 139.

[17] J. Nuyts et al., *Iterative reconstruction for helical CT: a simulation study*, *Phys. Med. Biol.* **43** (1998) 729.

[18] E.U. Mumcuoglu, R. Leahy, S.R. Cherry and Z. Zhou, *Fast gradient-based methods for Bayesian reconstruction of transmission and emission PET images*, *IEEE Trans. Med. Imag.* **13** (1994) 687.

[19] K. Van Slambrouck and J. Nuyts, *Reconstruction Scheme for Accelerated Maximum Likelihood Reconstruction: The Patchwork Structure*, *IEEE Trans. Nucl. Sci.* **61** (2014) 173.

[20] C. Watson, *Extension of Single Scatter Simulation to Scatter Correction of Time-of-Flight PET*, *IEEE Trans. Nucl. Sci.* **54** (2007) 1679.

[21] M.E. Werner, S. Surti and J.S. Karp, *Implementation and Evaluation of a 3D PET Single Scatter Simulation with TOF Modeling*, in the proceedings of the *IEEE Nuclear Science Symposium Conference Record*, San Diego, CA, U.S.A., 29 October–1 November 2006, pp. 1768-1773 [DOI:10.1109/nssmic.2006.354238].

[22] S. Alenius and U. Ruotsalainen, *Generalization of median root prior reconstruction*, *IEEE Trans. Med. Imag.* **21** (2002) 1413.

[23] R. Boellaard, M.B.M. Hofman, O.S. Hoekstra and A.A. Lammertsma, *Accurate PET/MR Quantification Using Time of Flight MLAA Image Reconstruction*, *Mol. Imaging. Biol.* **16** (2014) 469.

[24] A. Lougovski et al., *A volume of intersection approach for on-the-fly system matrix calculation in 3D PET image reconstruction*, *Phys. Med. Biol.* **59** (2014) 561.

[25] S. Jan et al., *GATE: A Simulation toolkit for PET and SPECT*, *Phys. Med. Biol.* **49** (2004) 4543 [physics/0408109].

[26] V. Bettinardi et al., *Physical Performance of the new hybrid PET/CT Discovery-690*, *Med. Phys.* **38** (2011) 5394.

[27] P. Lecoq, *On the way to the 10 ps time-of-flight PET challenge*, *Eur. Phys. J. Plus.* **137** (2022) 964.

[28] M.S. Lee, J.W. Cates, A. Gonzalez-Montoro and C.S. Levin, *High-resolution time-of-flight PET detector with 100 ps coincidence time resolution using a side-coupled phoswich configuration*, *Phys. Med. Biol.* **66** (2021) 125007.

[29] A. Rezaei et al., *Simultaneous Reconstruction of Activity and Attenuation in Time-of-Flight PET*, *IEEE Trans. Med. Imag.* **31** (2012) 2224.

[30] H. Hemmati, A. Kamali-Asl, P. Ghafarian and M.R. Ay, *Mixture model based joint-MAP reconstruction of attenuation and activity maps in TOF-PET*, 2018 *JINST* **13** P06005.

2023 JINST 18 P09041